

Clustered frequency analysis of shear Alfvén modes in stellarators

D. A. Spong,¹ E. D'Azevedo,¹ and Y. Todo²

¹*Oak Ridge National Laboratory, Oak Ridge, Tennessee 37831-6169, USA*

²*National Institute for Fusion Science, Oroshi-cho 322-6, Toki-city, 509-5292 Gifu, Japan*

(Received 10 September 2009; accepted 20 January 2010; published online 24 February 2010)

The shear Alfvén spectrum in three-dimensional configurations, such as stellarators and rippled tokamaks, is more densely populated due to the larger number of mode couplings caused by the variation in the magnetic field in the toroidal dimension. This implies more significant computational requirements that can rapidly become prohibitive as more resolution is requested. Alfvén eigenfrequencies and mode structures are a primary point of contact between theory and experiment. A new algorithm based on the Jacobi–Davidson method is developed here and applied for a reduced magnetohydrodynamics model to several stellarator configurations. This technique focuses on finding a subset of eigenmodes clustered about a specified input frequency. This approach can be especially useful in modeling experimental observations, where the mode frequency can generally be measured with good accuracy and several different simultaneous frequency lines may be of interest. For cases considered in this paper, it can be a factor of 10^2 – 10^3 times faster than more conventional methods. © 2010 American Institute of Physics. [doi:[10.1063/1.3313818](https://doi.org/10.1063/1.3313818)]

I. INTRODUCTION

Energetic particle (EP) destabilized coherent Alfvén modes have been observed in nearly all stellarator experiments, beginning with the Wendelstein 7-AS (W7-AS) (Ref. 1) and more recently including the compact helical system (CHS),² large helical device (LHD),³ flexible heliac (TJ-II),⁴ heliotron-J,⁵ and helical system experiment (HSX).⁶ A wide phenomenology of Alfvén mode activity has been identified, including global Alfvén eigenmodes, toroidal Alfvén eigenmodes (TAEs), helical Alfvén eigenmodes (HAEs), energetic particle modes (EPM), and reversed shear Alfvén eigenmodes (RSAEs). Both regimes with benign effects on fast particle confinement have been seen, as well as those with enhanced losses. These instabilities have also been extensively observed on tokamaks;⁷ they are driven by wave-particle resonant interactions (inverse Landau damping) between EP populations and otherwise neutrally stable Alfvén eigenmodes. For instability, several conditions must be satisfied: the EP velocity must be of the order of the wave phase velocity ($\sim v_{\text{Alfvén}}$); the EP diamagnetic frequency should exceed the wave frequency; and the EP drive (e.g., from the spatial pressure gradient) should exceed damping mechanisms that are present. An important starting point both for studies of Alfvén stability and the simulation of EP confinement in the presence of these modes is the calculation of the Alfvén continuum and eigenmode structure. For weakly driven regimes near marginal stability, it is expected that the ideal magnetohydrodynamics (MHD) mode structure will not be strongly distorted by the EP component; this assumption has been the basis for a number of perturbative stability models, such as NOVA-K (Ref. 8) (for tokamaks) and CAS3D-K (Ref. 9) (for stellarators) that have been useful for the identification of stability thresholds. In this paper a computational model (AE3D) is described for the calculation of Alfvén

eigenmodes in fully three-dimensional equilibria; improved performance has been achieved by use of a Jacobi–Davidson algorithm that selects a limited number of eigenmodes centered about a specified target frequency. A related method has been applied to the calculation of the MHD spectrum for axisymmetric (tokamak) equilibria.¹⁰ In conjunction with AE3D, the STELLGAP code¹¹ is used to provide Alfvén continua. The new clustered-frequency solution method presented here for stellarators has been motivated by several characteristics that are unique to Alfvén instabilities. First, these are modes with finite real frequencies, several of which may be simultaneously driven; thus, unlike conventional ideal MHD, more than just the mode with the minimum value of ω^2 is typically of interest. Second, the most readily obtained experimental signature of such modes is their real frequency, which can be measured dynamically and with good accuracy. Finally, the computation of such modes in three-dimensional systems can rapidly become unwieldy as increasing resolution and physics requirements are added, resulting in a need for more efficient algorithms. Although the application of the Jacobi–Davidson algorithm is presented here for stable incompressible shear Alfvén modes, this method is readily extendable to modes with complex eigenvalues, such as will result if either damping effects (kinetic Alfvén wave coupling, resistivity, viscosity, etc.) or EP destabilizing effects are added to the moment equations that are used here. While the computational challenges of finding Alfvén eigenmodes can also be addressed by parallel methods, the (single processor) approach described here is expected to be useful for applications such as analysis of time-varying experimental data, stellarator optimization, and preconditioning of more comprehensive models. The clustered frequency approach can also be parallelized, as will be discussed further in Sec. III.

II. ANALYSIS

The new solution technique described in this paper will be illustrated for a model problem, namely, a reduced MHD model of shear Alfvén waves in three-dimensional toroidal plasmas. The approximations used here are applicable to the subset of Alfvén instabilities that are not significantly modified by coupling to the acoustic (parallel compressibility) waves or the fast (magnetosonic) waves. The full coupled shear Alfvén/acoustic/magnetosonic MHD mode spectrum has previously been treated in the CAS3D model,¹² which is based on a δW /plasma displacement approach. While the Jacobi–Davidson solution technique described here should also be quite useful for analysis of modes affected by these couplings, this extension will be left for future work.

The equations used here are based on a reduced MHD derivation¹³ that uses a multiple time- and length-scale expansions to obtain moment equations that are valid for general toroidal configurations at arbitrary aspect ratio. The primary ordering assumed is that k_{\parallel}/k_{\perp} is a small parameter (k_{\parallel} , k_{\perp} =wavenumbers parallel and perpendicular to the magnetic field). Equations (49) and (50) from Ref. 13 are used for a basic description of shear Alfvén waves; resistivity, pressure anisotropy, and pressure gradient terms are neglected. This eliminates pressure gradient-driven modes and resistive tearing modes, which again are not directly relevant to the shear Alfvén modes that are of interest here. The basic equations then are the ideal Ohm's law and vorticity equation as given below,

$$\frac{\partial \tilde{\psi}}{\partial t} = \frac{1}{B} (\mathbf{B} \cdot \nabla) \phi,$$

$$\nabla \cdot \left(\frac{\mu_0 \rho_m}{B} \frac{d}{dt} \frac{\nabla \phi}{B} \right) = (\mathbf{B} \cdot \nabla) \frac{\tilde{J}_{\parallel}}{B} + (\tilde{\mathbf{B}} \cdot \nabla) \frac{J_{\parallel 0}}{B}, \quad (1)$$

with

$$\tilde{J}_{\parallel} = \nabla^2 \psi, \quad \tilde{\mathbf{B}} = \nabla \zeta \times \nabla \tilde{\psi}. \quad (2)$$

Here \mathbf{B} is the equilibrium magnetic field, B is its magnitude, \tilde{J}_{\parallel} is the perturbed parallel current, $J_{\parallel 0}$ is the equilibrium parallel current, ϕ is the electrostatic potential, $\tilde{\psi}$ is the perturbed flux function, ζ is the toroidal angle coordinate, $\rho_m = m_{\text{ion}} n_{\text{ion}}$ is the ion mass density, and μ_0 =free space permeability= $4\pi \times 10^{-7}$ H/m. Assuming an $e^{-i\omega t}$ time dependence and combining Eqs. (1) and (2) results in the eigenvalue equation

$$\begin{aligned} \omega^2 \nabla \cdot \left(\frac{1}{v_A^2} \nabla \phi \right) + (\mathbf{B} \cdot \nabla) \left[\frac{1}{B} \nabla^2 \left(\frac{\mathbf{B}}{B} \cdot \nabla \phi \right) \right] \\ + \nabla \zeta \times \nabla \left(\frac{\mathbf{B}}{B} \cdot \nabla \phi \right) \cdot \nabla \frac{J_{\parallel 0}}{B} = 0, \end{aligned} \quad (3)$$

where $v_A^2 = B^2 / \mu_0 \rho_m$. Equation (3) is multiplied by a trial function $\tilde{\phi}$ and integrated over the volume of the plasma. Integration by parts is used and divergence terms are neglected based on the boundary conditions that ϕ and $\tilde{\phi}$ are set=0 on the plasma edge. This results in the equation given below,

$$\begin{aligned} -\omega^2 \int d^3x \frac{1}{v_A^2} \nabla \tilde{\phi} \cdot \nabla \phi \\ + \int d^3x \left[\nabla \left(\frac{\mathbf{B} \cdot \nabla \tilde{\phi}}{B} \right) \cdot \nabla \left(\frac{\mathbf{B} \cdot \nabla \phi}{B} \right) \right] \\ + \int d^3x \left(\frac{\mathbf{B} \cdot \nabla \phi}{B} \right) \nabla \zeta \cdot \nabla \tilde{\phi} \times \nabla \left(\frac{J_{\parallel 0}}{B} \right) = 0. \end{aligned} \quad (4)$$

Equation (4) is then solved using the Galerkin approach, whereby ϕ is expanded in a finite dimensional set of basis functions. The same basis functions are then used sequentially for the trial function $\tilde{\phi}$, resulting in the generation of a matrix eigenvalue equation. Specifically, we use a hybrid Fourier series/finite element representation. Boozer magnetic coordinates¹⁴ (ρ, θ, ζ) are used where ρ is a radiuslike flux surface label, θ is the poloidal angle variable, and ζ is a toroidal angle variable. Due to the choice of Jacobian, ζ does not correspond to the usual cylindrical angular coordinate and will generally have a nonuniform spacing when projected to real space. In these coordinates the magnetic field and volume element have the forms

$$\mathbf{B} = \chi' \nabla \rho \times \nabla \theta + \psi' \nabla \zeta \times \nabla \rho,$$

$$d^3x = \sqrt{g} d\rho d\theta d\zeta; \quad (5)$$

$$\sqrt{g} = [\nabla \rho \cdot (\nabla \theta \times \nabla \zeta)]^{-1} = \chi' (G + iI) / B^2,$$

where θ =poloidal angle, ζ =toroidal angle, χ =toroidal magnetic flux function, ψ =poloidal magnetic flux function, ρ =flux surface coordinate (taken as χ'/χ_{edge} here), i =rotational transform= ψ'/χ' , with primes denoting $d/d\rho$, and I, G =toroidal/poloidal currents. ϕ and $\tilde{\phi}$ are represented as

$$\phi = \sum_{i=1}^I \sum_{p=1}^P \phi_{ip} f_p(\rho) \cos(m_i \theta - n_i \zeta);$$

$$\tilde{\phi} = f_q(\rho) \cos(m_j \theta - n_j \zeta);$$

$$\text{with } 1 \leq q \leq P \quad \text{and} \quad 1 \leq j \leq I,$$

where $f_p(\rho)$ is a finite element basis function. In the case of linear finite elements, which have been used here for solving Eq. (4), $f_p(\rho)$ is represented as

$$f_p(\rho) = \begin{cases} \frac{\rho - \rho_{p-1}}{\rho_p - \rho_{p-1}} & \rho_{p-1} \leq \rho \leq \rho_p \\ \frac{\rho_p - \rho}{\rho_p - \rho_{p-1}} & \rho_p \leq \rho \leq \rho_{p+1} \\ 0 & \rho < \rho_{p-1} \text{ or } \rho > \rho_{p+1}. \end{cases} \quad (6)$$

Note that the above Fourier representation for ϕ assumes that the equilibrium magnetic field is characterized by stellarator symmetry, i.e., that B can be represented by a cosine series: $B = \sum_{m,n} B_{mn} \cos(m\theta - n\zeta)$. This is equivalent to the condition $\phi_{m,n} = \phi_{-m,-n}$ that would apply if a complex Fourier representation were used: $\phi \propto e^{i(m\theta - n\zeta)}$. However, it is noted that the model used here and solution techniques can readily be gen-

eralized by including the appropriate $\sin(m\theta - n\zeta)$ terms in the above representations. This would be necessary, for example, for application to nonstellarator-symmetric configurations or if certain forms of kinetic gyrofluid closure relations¹⁵ were used to include the EP destabilization. Using the above forms for ϕ and $\tilde{\phi}$ in Eq. (4) then leads to a generalized eigenvalue problem as given below,

$$\mathbf{F}\mathbf{y} = \lambda\mathbf{G}\mathbf{y}, \quad (7)$$

where $\lambda = \omega^2$ and details of the matrices \mathbf{F} and \mathbf{G} are given in the Appendix. \mathbf{y} is a column vector composed of the amplitudes ϕ_{ip} . These are typically ordered with the Fourier mode index i , being the innermost rapidly varying loop, and the finite element radial index p , being the outermost more slowly varying loop. This ordering results in block tridiagonal matrices with the block size determined by I , the number of Fourier modes, and the number of blocks along the main diagonal determined by P , the number of finite element basis functions.

III. EIGENMODE SOLUTION METHODS

The shear Alfvén eigenmode problem [Eq. (5)] and Fourier/finite element representation described in Sec. II leads to a sparse symmetric structure for the matrices \mathbf{G} and \mathbf{F} with large dense tridiagonal blocks. Several different options have been developed for solving this system. The first and most straightforward is to simply solve for all of the eigenvalues and eigenvectors using standard LAPACK (Ref. 16) routines. The DGGEV generalized eigenvalue subroutine has been used for this purpose; DGGEV solves the generalized eigenvalue problem given in Eq. (7) by computing the generalized Schur decomposition (QZ algorithm). The routine can return the complete decomposition but it requires $O(N^3)$ work, where N is the size of the dense matrices \mathbf{F} , \mathbf{G} . This method becomes very expensive for N larger than about 2000. In our case, we have solved problems with up to 40 radial grid points and 243 Fourier modes (i.e., a problem size of about 10 000). It is also applicable to nonsymmetric matrices that will result when nonideal effects (resistivity, gyroviscosity, etc.) are included in this problem.

The second, higher performance option uses a Jacobi–Davidson style QZ algorithm.¹⁷ The Jacobi–Davidson method is similar to the Lanczos or Arnoldi methods in constructing a subspace where the given eigenproblem is projected. The difference is the subspace is generated using approximate shift-and-invert steps and may not be a proper Krylov subspace. Further details of the Jacobi–Davidson method may be found in Ref. 18. This approach significantly reduces the amount of work by calculating only a subset of eigenmodes that are clustered around a prespecified frequency determined by the user. The Jacobi–Davidson method has also been applied previously for computation of the MHD spectrum for tokamak plasmas.¹⁰ The approach used here is based on the JDQZ algorithm for generalized eigenproblems, which first transforms the eigenequation to the generalized Schur form by the QZ method,¹⁹ and then employs iterative methods that avoid the explicit inversion of the operators. It has the advantage that the full matrices do

not have to be formed in memory as they must for the DGGEV subroutine; routines are required that return matrix-vector products of the \mathbf{F} and \mathbf{G} matrices for arbitrary vectors. Since both \mathbf{F} and \mathbf{G} are generally sparse, this can allow larger problems to be addressed. In addition, a preconditioner for $\mathbf{F} - \tau\mathbf{G}$ must be provided by the user, where τ is the prespecified target eigenfrequency; for the problem addressed in this paper, a lower-upper (LU) decomposition has been found to be an effective preconditioning method. Other specific choices and parameters that have been used for the JDQZ algorithm are the following. GMRES has been used for the linear equation solver with a search-space dimension of 99; a cluster of 40 eigenmodes about the target frequency is typically requested (although this number can be varied); up to 200 Jacobi–Davidson iterations are allowed; the harmonic Petrov test-space expansion method is used; and tolerance and tracking parameters of 10^{-9} have been chosen.

The JDQZ algorithm only requires an algorithm to compute the matrix vector products $\mathbf{F}\mathbf{x}$, $\mathbf{G}\mathbf{x}$ and a preconditioner that returns an approximation of $(\mathbf{F} - \tau\mathbf{G})^{-1}\mathbf{x}$, thus it is possible to render a “matrix-free” implementation. In our actual implementation, the block tridiagonal matrices \mathbf{F} , \mathbf{G} are explicitly generated and stored in a compact form. The matrix-vector products are then efficiently performed using dense matrix operations. This structure has been used for the code due to its evolution from a full spectral solver based on the DGEEV routine and for ease in benchmarking between the two methods. In the future, the implementation will be converted to a matrix-free form.

With regard to parallelization of the JDQZ algorithm, there are several options. On a machine with multiple cores, one may invoke OPENMP compiler directives or multi-threaded basic linear algebra subroutine (BLAS) libraries to distribute the computation of the matrix-vector multiplies. If the number of Fourier modes is sufficiently high, SCALAPACK and parallel BLAS (PBLAS) may also be used to distribute the large dense sub-blocks across multiple processors. Moreover, a matrix-free algorithm may be an option where the radial grid is distributed across multiple processors and the matrix-vector product is reassembled using explicit communication.

IV. APPLICATIONS

In this section the model and algorithm described in Secs. II and III will be applied to a range of different stellarator configurations. Although many eigenmodes result from this calculation, only limited frequency ranges are typically of relevance (based either on the locations of open gap regions or experimental measurements). Also, experiments often provide information regarding mode structure and mode numbers. After discarding modes that do not fit these categories as well as those with strong continuum interactions (characterized by localized radial structures), there are generally only a few eigenmodes remaining. These are the cases that will be presented as examples in this section.

A. LHD TAE mode

As a first example of the above method, a low magnetic field discharge from the LHD experiment in which Alfvénic

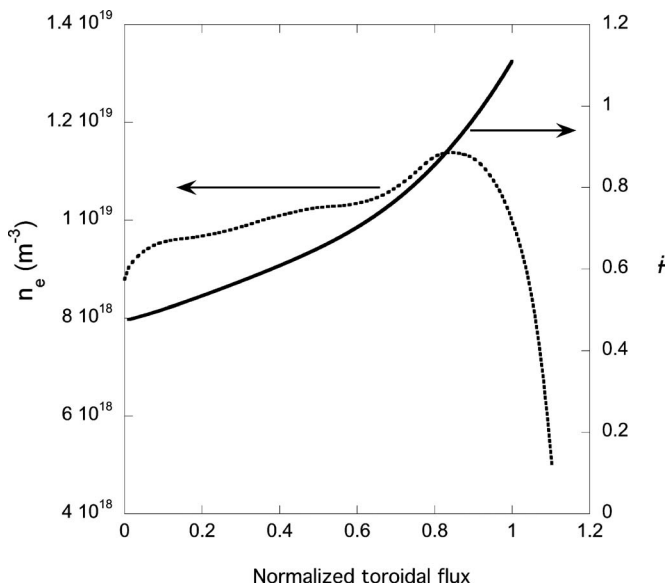


FIG. 1. Ion density and rotational transform profiles for LHD TAE mode example.

activity was present²⁰ has been chosen. This is selected from a series of cases that was used to study hole-clump formation related with Alfvén mode activity.²⁰ Eigenfunctions obtained from an earlier version of the AE3D model described here have previously been used in modeling the TAE bursts,²¹ indicating a reasonable agreement with experimental observations. The specific discharge considered is 47645; this was at low magnetic field strength (the volume-averaged field was ~ 0.8 T), allowing order unity ratios of beam ion velocity (180 keV hydrogen beams) to Alfvén velocity to be attained. The magnetic axis position was shifted out at $R_{\text{axis}} = 3.88$ m with a somewhat hollow ion density profile and a rotational transform profile that varied from 0.476 on the axis to 1.11 at the edge; these profiles are shown in Fig. 1. The STELLGAP code¹¹ has been used to obtain the shear Alfvén gap structure, as shown in Fig. 2. These are the eigenvalues of the equation formed by keeping only the highest order radial (ρ) derivative terms in Eq. (3); they are the continua of the shear Alfvén problem of Eq. (3) and provide guidance regarding the location and frequency ranges (the open gap regions) where eigenfunctions of the full equation that are characterized by a global radial structure will exist. For the model problem considered in this paper, the physics of continuum damping is not resolved, so the focus will be on eigenmodes whose frequency is in the open gap regions and that have relatively weak interaction with the continuum.

In Fig. 2(a) the Alfvén continua are first displayed for the case where only $|n|=1$ modes are included. Here, $n=-1$, $m=0-5$ modes are retained. For the equilibrium convention used for LHD, $\dot{\phi} < 0$ and $n < 0$ modes are those aligned with the magnetic field line helicity; in this case, $n > 0$ modes are only of importance at significantly higher frequencies than those shown in Fig. 2. In Fig. 2(b) the extension of the continua in Fig. 2(a) to the case multiple toroidal mode numbers is given. For Fig. 2(b), the modes $n=-1$, $m=0$ to 5; $n=-9$, $m=6$ to 30; and $n=-11$, $m=8$ to 36 are included.

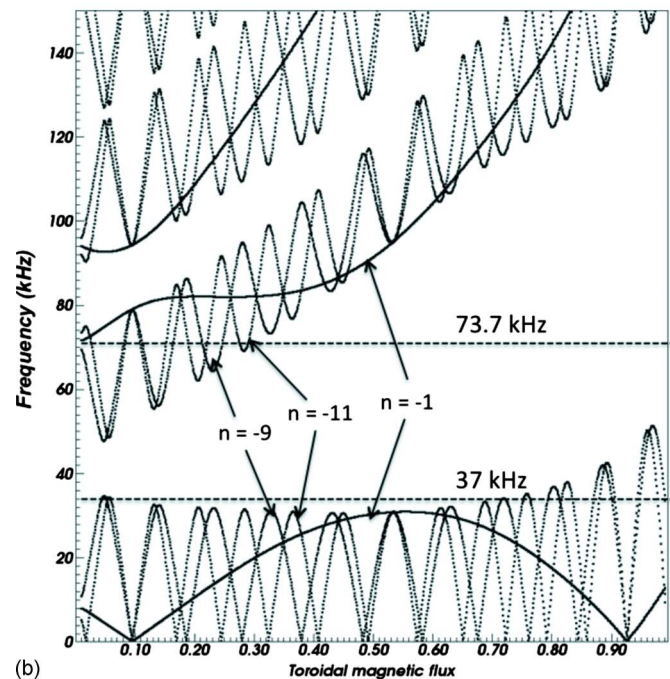
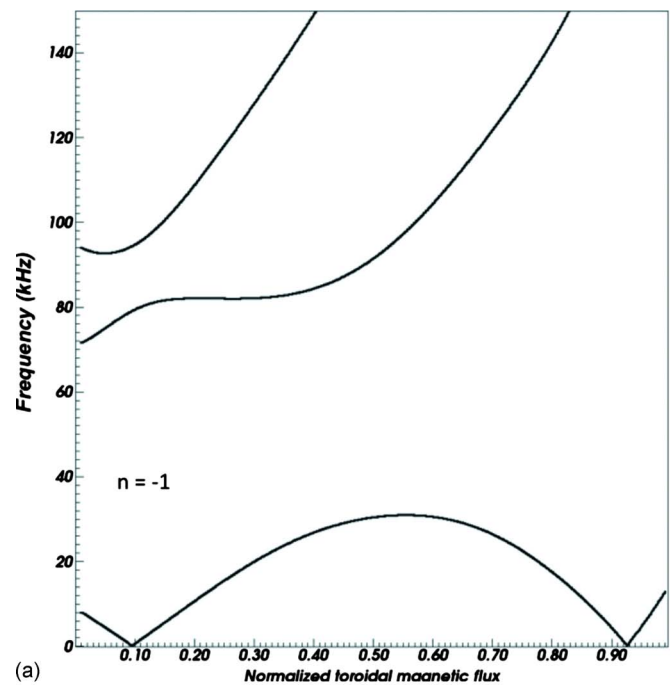


FIG. 2. (Color online) (a) $n=-1$ continua for LHD TAE example based on $n=-1$, $m=0-5$ modes; (b) same as (a), but including additional couplings to $n=-9$, $m=6-30$ and $n=-11$, $m=8-36$ modes.

These toroidal modes follow the $n=-1$ mode family selection rules^{12,22} that include toroidal modes that are displaced from $n=+1$ by adding and subtracting integral multiples of the field period N_{fp} (in the case of LHD $N_{\text{fp}}=10$). While the addition of the $n=-9$ and $n=-11$ modes would appear to significantly narrow the primary gap, the influence of these new continua on the damping of the $n=-1$ modes will depend on the strength of the mode coupling between eigenfunctions dominated by $n=-1$ and the higher order n 's.

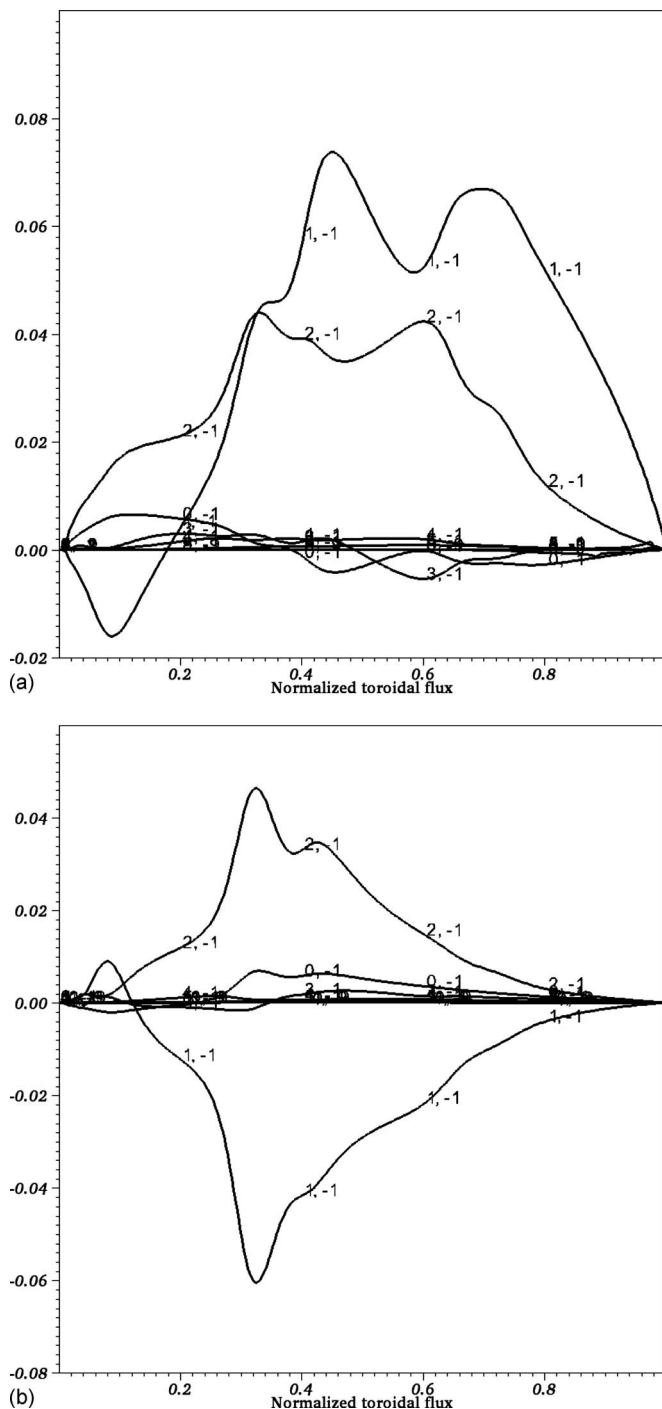


FIG. 3. Radial eigenmode structure for (a) LHD 37 kHz mode and (b) 73.7 kHz mode.

As may be seen, the coupling of the $n=-1$ with the $n=-9$ and -11 modes has made relatively little change in the $n=-1$ continua between Figs. 2(a) and 2(b).

As indicated in Fig. 2(a) by horizontal dashed lines, two eigenfunctions have been found in this frequency range at 37 and 73.7 kHz with relatively global radial mode structure. The radial eigenmodes (ϕ_{mn}) for these are plotted in Figs. 3(a) and 3(b). The 37 kHz mode is dominated by $(m, n) = 1, -1$ and $2, -1$ components that are in phase and shows minor effects of continuum crossing near the edge. The 73.7 kHz mode is also $(m, n) = 1, -1$ and $2, -1$ dominated,

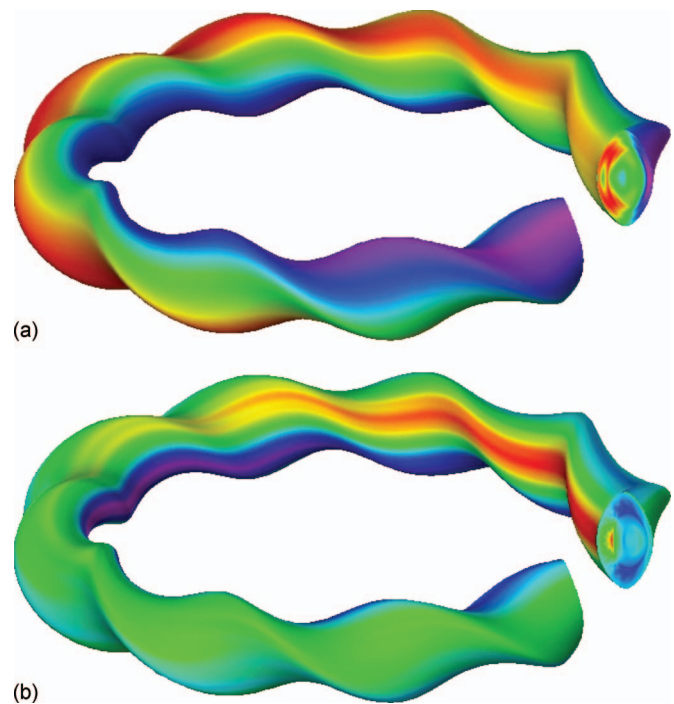


FIG. 4. (Color) Three-dimensional eigenmode structure for (a) LHD 37 kHz mode (top image) and (b) 73.68 kHz mode (bottom image). The color contours correspond to the magnitude of the potential with magenta representing the minimum value and red representing the maximum value.

with the two modes having opposite phases. In Fig. 4, the three-dimensional structure of these eigenmodes is displayed for a magnetic flux surface at 80% of the edge magnetic flux. The color contours indicate the value of the potential on that surface with magenta representing the minimum value and red representing the maximum value. The mode frequencies are in a similar range as the experimental observations; differences result from the fact that the plasma $\mathbf{E} \times \mathbf{B}$ rotation and effective ion mass (both of which influence the predicted frequency) are not well known.

The Jacobi–Davidson cluster eigenvalue solution method described in Sec. III has been applied to this case, resulting in very close agreement with the eigenvalues and eigenmodes obtained using the LAPACK generalized full eigenmode solver, DGGEV. An example of this agreement between the cluster and full solution approaches is shown in Fig. 5, where a scan has been made in the target frequencies. In the right-hand side of the plot (to the right of the dashed line), all of the eigenvalue frequencies obtained from the DGGEV routine in the frequency range from 30 to 80 kHz are indicated. To the left of the dashed line the clusters of 40 eigenvalues provided by the Jacobi–Davidson solver are plotted as the target frequency is varied from 34 to 70 kHz. There is a close agreement between the individual Jacobi–Davidson and DGGEV eigenfrequencies and also an agreement between the adjacent overlapping Jacobi–Davidson results. Typically, the relative frequency deviation between the two methods $|\text{frequency}(\text{DGGEV}) - \text{frequency}(\text{JQDZ})| / \text{frequency}(\text{DGGEV})$ is in the range of 10^{-5} – 10^{-7} . For the data in Fig. 5, the mean relative difference was 1.01×10^{-6} .

In Fig. 6 we plot the performance comparisons for the

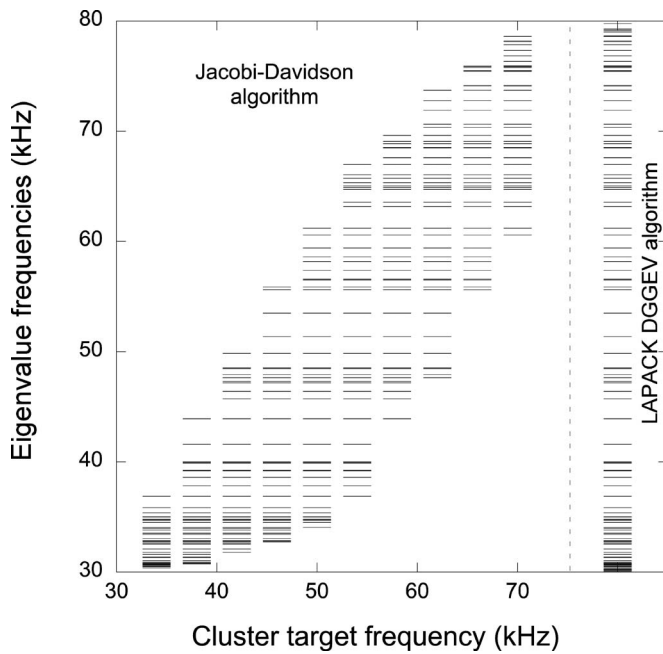


FIG. 5. Comparison of eigenvalues ($\omega/2\pi$) from Jacobi-Davidson algorithm with different target frequencies and those from the LAPACK DGGEV algorithm.

two methods along with the time required to construct the matrices as the problem size is varied. These results were obtained on a 64 bit Linux workstation with an Intel Xeon Quad Core (E5335) 2 GHz processor using the GFORTRAN compiler. The number of radial grid points varied from 39 to 59 and the number of Fourier modes was varied from 12 to 243. These results indicate that the JDQZ solver is substantially faster than the full eigenvalue DGGEV solver and has a more favorable scaling with increasing problem size.

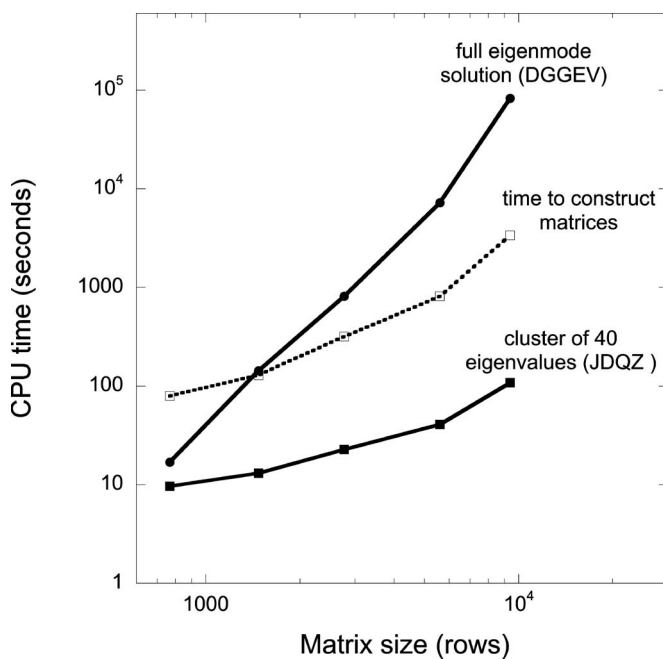


FIG. 6. Performance comparison between DGGEV and JDQZ algorithm along with time for the construction of the \mathbf{G} and \mathbf{F} matrices.

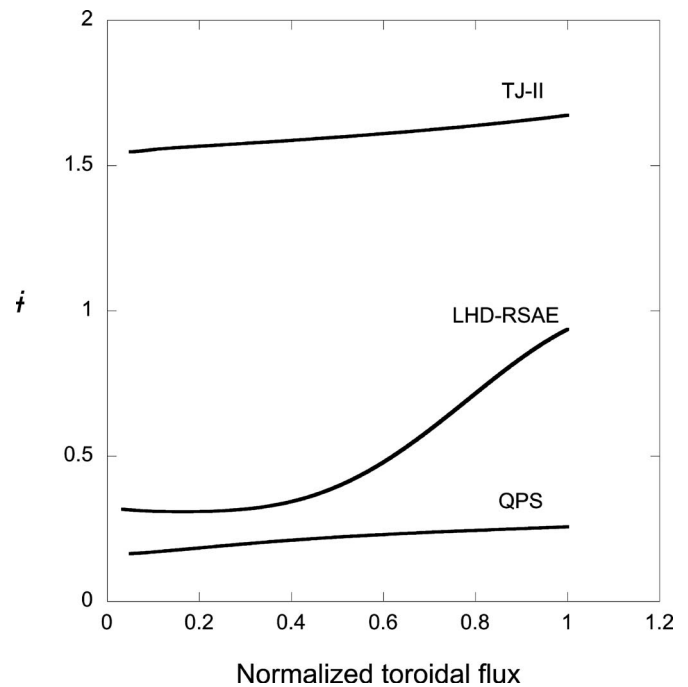


FIG. 7. Rotational transform profiles for TJ-II, nonmonotonic LHD RSAE, and QPS cases.

In Secs. IV B–IV D, further example configurations are presented where the use of the JDQZ clustered frequency algorithm has significantly facilitated the identification of Alfvén eigenmodes that have weak continuum interactions.

B. LHD RSAE mode

A second example of EP-driven modes that have recently been observed in LHD is the reversed shear Alfvén (RSAE) mode.²³ Such modes are possible when the rotational transform profile has a nonmonotonic variation, as can be produced by beam current drive and appropriate startup programming. LHD transform profiles have been created²³ with a minimum near the half-radius (~ 0.2 in the normalized flux variable used in this paper). For this case, $\langle B \rangle = 1.3$ T, $n(0) = 5 \times 10^{18} \text{ m}^{-3}$, $m_i/m_p = 1.5$, and $i = 0.32\text{--}0.95$ with $i_{\min} = 0.309$. The rotational transform profiles for this case and the remaining two example configurations are plotted in Fig. 7. Using a set of model profiles, the continua for the $|n|=1$ mode family are plotted in Fig. 8. Four $n=-1$ dominated modes with a global radial mode structure are found in the first gap above the lower $n=-1$ continuum and below the upper $n=-1$ continuum, as indicated by the dashed lines. For the $n=-1$ mode family eigenmode analysis, 160 radial points were used and 95 Fourier modes, consisting of $n = \pm 1$ ($m = 0\text{--}12$), $n = -9$ ($m = 5\text{--}38$), and $n = -11$ ($m = 5\text{--}40$). In Fig. 9 the eigenmode structures associated with the four modes indicated in Fig. 8 are plotted. RSAE modes in tokamaks are typically dominated by a single poloidal mode. This is apparent for the 64.9 and 88.1 kHz modes, which are $(m, n) = (3, -1)$ dominated; the 49.7 and 101.6 kHz modes show couplings between several poloidal modes. For clarity, not all modes included in the calculation are plotted here. For Fig. 9(a) evidence of continuum interaction can be seen in the

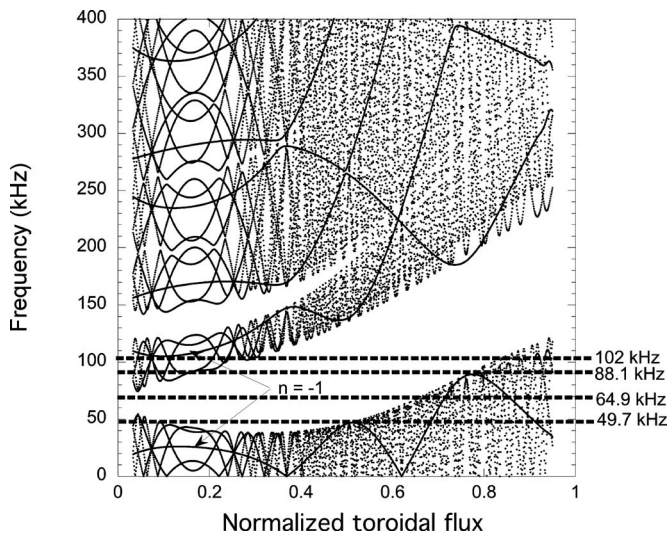


FIG. 8. Shear Alfvén continuum structure for LHD with a nonmonotonic rotational transform profile.

(1, -1) mode, but is at a low level compared with the main (3, -1) mode. Mode structures have been chosen in Fig. 9 that are radially dominant near the first local maximum in the lower $n=-1$ continuum and the local minimum in the upper $n=-1$ continuum. In Fig. 10 the global three-dimensional structure of the 88.1 kHz RSAE mode of Fig. 9(c) is shown.

Both of the above LHD examples are dominated by a single toroidal mode number, with only weak coupling to adjacent n 's. As mentioned above, this characteristic is due to the high field symmetry ($N_{fp}=10$), relatively high aspect ratio and moderate helical curvature that characterize this configuration. These characteristics result in Alfvén mode structures that share certain similarities to those found in tokamaks. While Alfvén modes with helical coupling characteristics have been found in LHD,²⁴ they tend to occur at higher frequencies and near the edge regions. Next, examples will be given of lower field period configurations having either strong helical curvature (TJ-II) or very low aspect ratio [quasipoloidal stellarator (QPS)] where stronger helical and toroidal mode couplings will lead to Alfvén eigenmode structures that deviate more significantly from those of the tokamak.

C. TJ-II HAE mode

TJ-II is a four field period flexible heliac configuration that has reported⁴ neutral beam-driven $n/m=3/2$ Alfvén instabilities in the 150–300 kHz regime. Using modeled profiles and parameters that characterize this regime, the Alfvén continua given in Fig. 11 are obtained. For this case, $\langle B \rangle = 1.0$ T, $n(0)=3 \times 10^{19}$ m⁻³, $m_i/m_p=1.0$, and $i=1.55$ –1.68 (full rotational transform profile was given in Fig. 7). Eigenmodes with weak continuum coupling have been found in the lowest gap at 148 kHz [Fig. 12(a)] and in the second gap at 330 kHz [Fig. 12(b)]. For this calculation 40 radial points were used and 243 Fourier modes, consisting of $n=\pm 1$ ($m=0$ –10), $n=\pm 3$ ($m=0$ –12), $n=\pm 5$ ($m=1$ –14), $n=\pm 7$ ($m=2$ –15), $n=-9$ ($m=3$ –17), $n=-11$ ($m=5$ –19), $n=-13$ ($m=6$ –20), $n=-15$ ($m=6$ –20), $n=-17$ ($m=7$ –22), $n=-19$

($m=8$ –23), $n=-21$ ($m=10$ –23), $n=-23$ ($m=9$ –24), and $n=-25$ ($m=10$ –25). The 148 kHz mode is dominated by the $-3/2$ helicity that was reported while the 330 kHz mode is dominated by an $n/m=-17/10$ helicity. The lower frequency mode is and HAE since it couples across different m 's and n 's. The higher frequency mode is more TAE-like since it couples (m,n)=(10, -17) and (11, -17) modes with weaker coupling to a (9, -13) mode. In the case of TJ-II these couplings can be attributed to the low number of field periods and strong helical variation in the configuration. The three-dimensional variation in the 330 kHz eigenmode is shown in Fig. 13.

D. QPS HAE mode

QPS is a very low aspect ratio ($\langle R \rangle / \langle a \rangle = 2.7$), low field period ($N_{fp}=2$) configuration whose design was based upon drift optimization and approximate quasipoloidal symmetry. For devices such as QPS and National Compact Stellarator Experiment (NCSX), due to their compact geometry, the Alfvén spectra become even more strongly coupled than either the LHD or TJ-II configurations that were considered above. In Fig. 14(a) the continua for the $n=1$ mode family are plotted. Here, $\langle B \rangle = 1.0$ T, $n(0)=3 \times 10^{19}$ m⁻³, $m_i/m_p=1.0$, and $i=0.16$ –0.26 (full rotational transform profile was given in Fig. 7). As can be seen, there is a wide primary gap present that ranges from about 50 to 140 kHz near the magnetic axis. Below this is a narrower gap with obliquely slanted gap regions intersecting it near normalized flux locations of 0.2, 0.3, 0.5, and 0.9. These can be interpreted as the “continuum-crossing gaps” that were identified by Yakovenko *et al.*²⁵ and are often found for low aspect ratio/low field period configurations. An example of a QPS Alfvén eigenmode with weak continuum interaction is shown in Fig. 14(b). This mode was found at 149 kHz and exists near the center of the large primary open gap, to which its very global $n/m=1/(3,4,5)$ mode structure can be attributed. Again for clarity not all of the modes included are plotted here. For the eigenmode calculation, 40 radial points were used with 66 Fourier modes, consisting of $n=1$ ($m=0$ –15), $n=3$ ($m=2$ –25), and $n=5$ ($m=5$ –30). The three-dimensional structure of this eigenmode is shown in Fig. 15.

V. CONCLUSIONS

A new method has been demonstrated for the rapid solution of shear Alfvén eigenfrequencies and mode structures in three-dimensional magnetic confinement systems such as stellarators and tokamaks with symmetry-breaking effects [field ripple, ferritic materials, resistive wall mode (RWM) coils, and other internal MHD instabilities]. This is based on the use of a Jacobi–Davidson technique that solves for a cluster of eigenvalues centered about a specified target frequency. This has been applied here for a reduced MHD model description of stable shear Alfvén eigenmodes, but is fully applicable to more general stability problems with complex eigenvalues, such as Alfvén modes destabilized by wave-particle resonances, resistive MHD, Alfvén modes with dissipative effects, and couplings between shear Alfvén and kinetic Alfvén modes. Improved performance for this

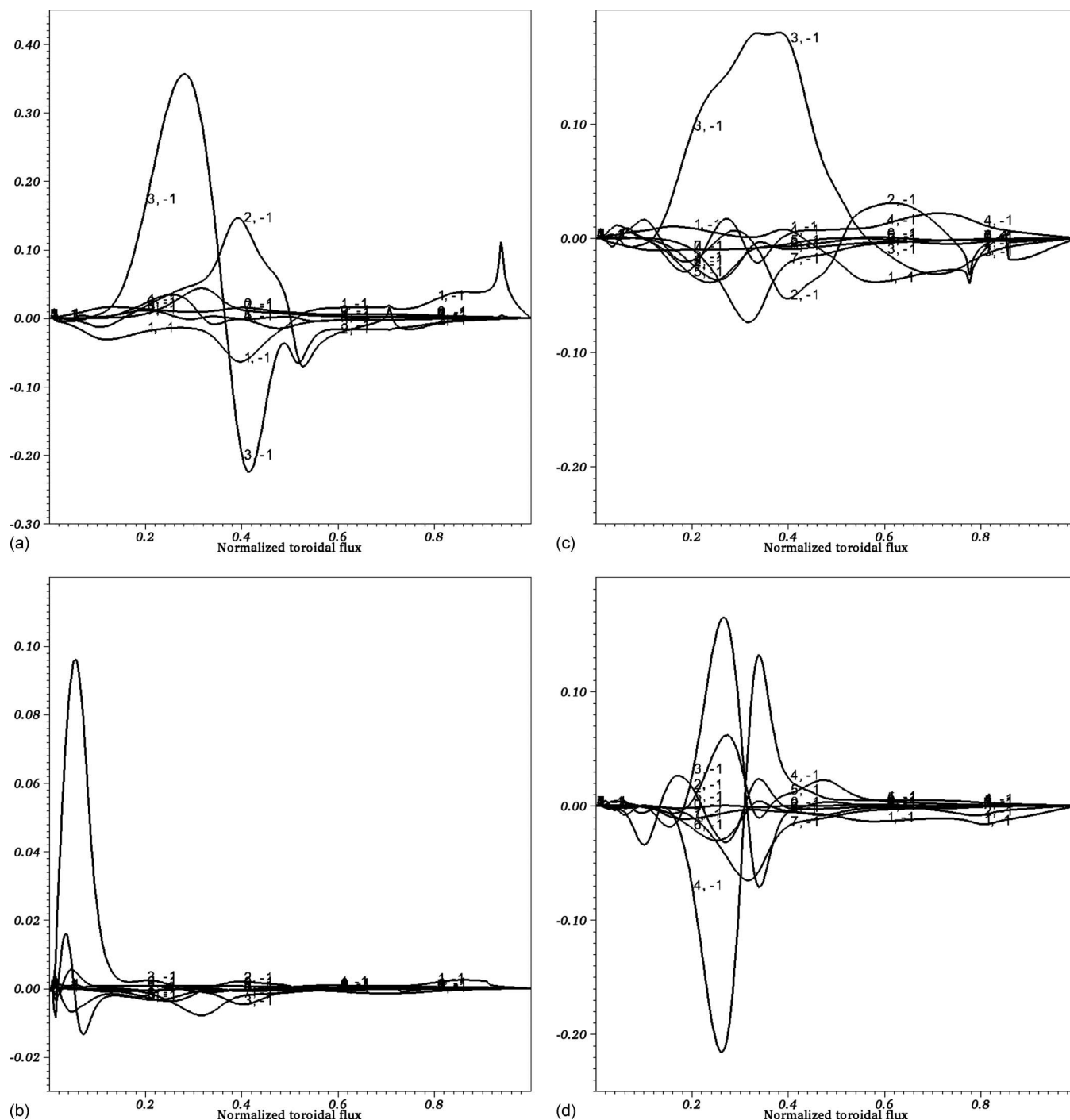


FIG. 9. Radial eigenmode structures for (a) 49.7, (b) 64.9, (c) 88.1, and (d) 101.6 kHz Alfvén eigenmodes modes that are localized near the inner gap region for LHD reversed shear case.

model problem is expected to be useful in perturbative models of these instabilities, stellarator optimization, and in benchmarking of more comprehensive codes.

The model described here has been applied to several discharges from the LHD and TJ-II experiments where Alfvén mode activity was observed. Eigenmodes with global radial structure are found near the observed frequencies and mode numbers. In addition, this model has been applied to low aspect ratio stellarators, such as QPS, where equally strong poloidal and toroidal couplings are present in the equilibrium flux surface shape.

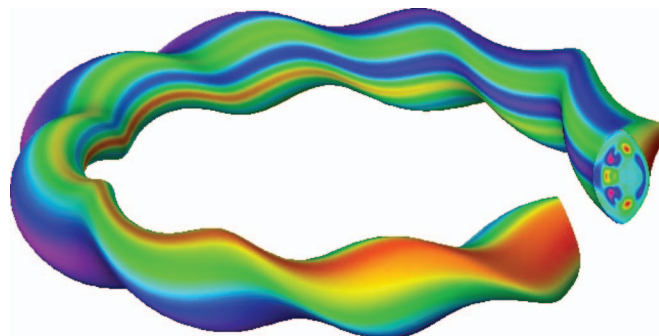
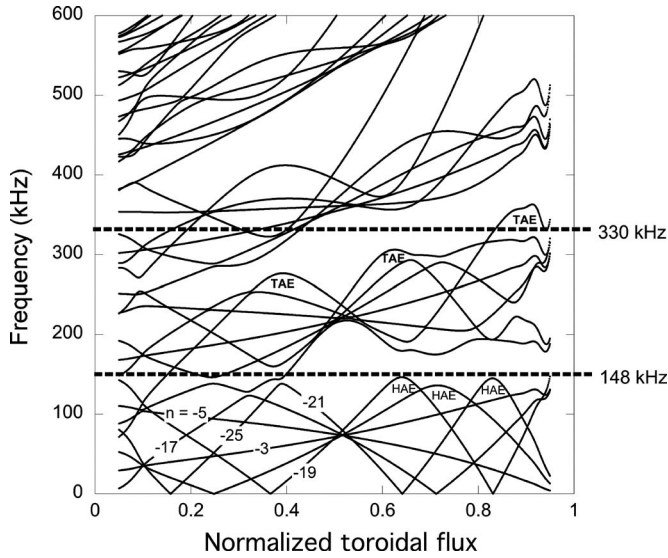


FIG. 10. (Color) Three-dimensional mode structure of LHD 88.2 kHz RSAE mode.

FIG. 11. TJ-II shear Alfvén continuum plot for $n=-1$ mode family.

ACKNOWLEDGMENTS

Research was sponsored by the U.S. Department of Energy under Contract No. DE-AC05-00OR22725 with UT-Battelle, LLC. Helpful assistance from Steven Hirshman in the use of the VMEC code is gratefully acknowledged. The initial development of this model was supported by a National Institute for Fusion Science visiting professorship for one of the authors (D.A.S.).

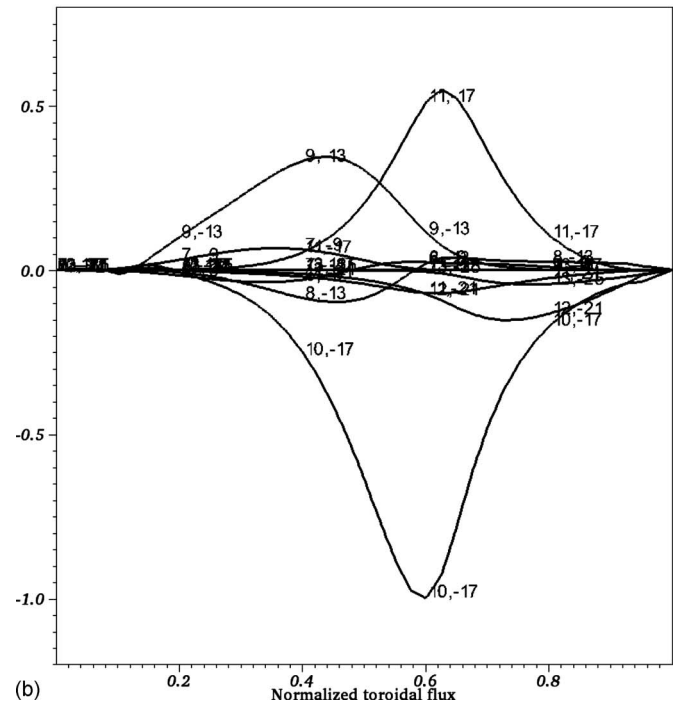
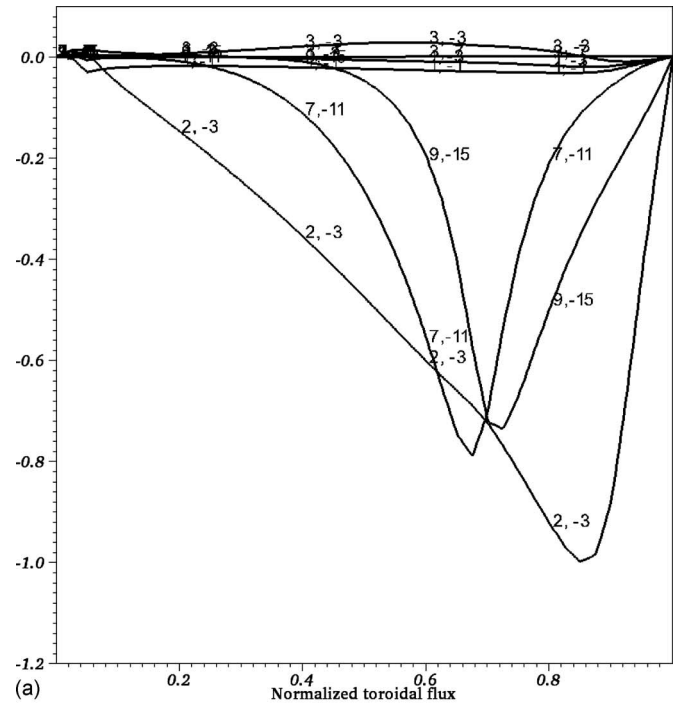
APPENDIX: EXPANSION OF MATRIX ELEMENTS IN MAGNETIC COORDINATES

The matrices \mathbf{F} and \mathbf{G} (representing inertia and field-line bending terms) in Eq. (5) are defined as follows:

$$\mathbf{G} \equiv \int d^3x \frac{1}{v_A^2} \nabla \tilde{\phi} \cdot \nabla \phi \quad \text{and}$$

$$\mathbf{F} = \int d^3x \left[\nabla \left(\frac{\mathbf{B} \cdot \nabla \phi}{B} \right) \cdot \nabla \left(\frac{\mathbf{B} \cdot \nabla \tilde{\phi}}{B} \right) \right. \\ \left. + \int d^3x \left(\frac{\mathbf{B} \cdot \nabla \tilde{\phi}}{B} \right) \nabla \zeta \cdot \nabla \tilde{\phi} \times \nabla \left(\frac{J_{||0}}{B} \right) \right].$$

Expanding the integrands in the magnetic curvilinear coordinate system that was described in Sec. II, one has



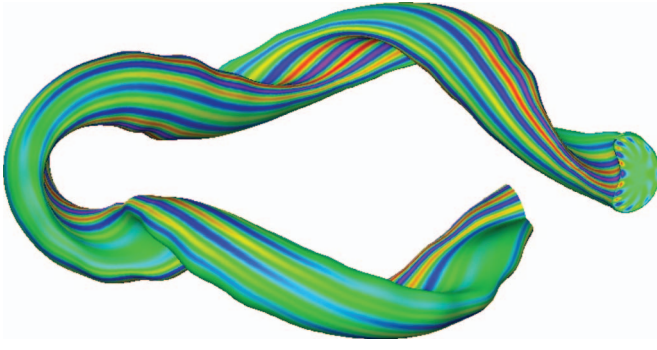


FIG. 13. (Color) Three-dimensional mode structure of TJ-II 330 kHz mode.

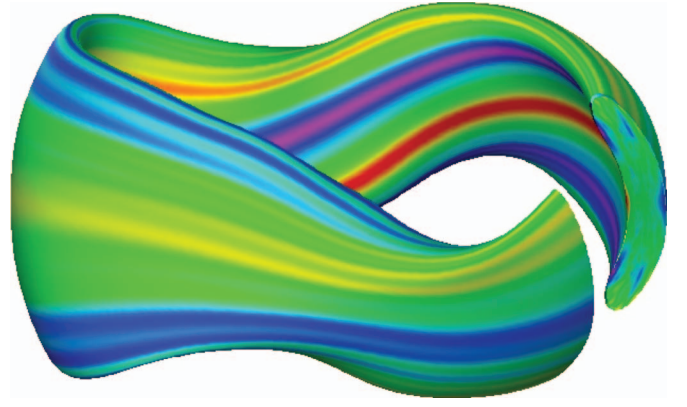
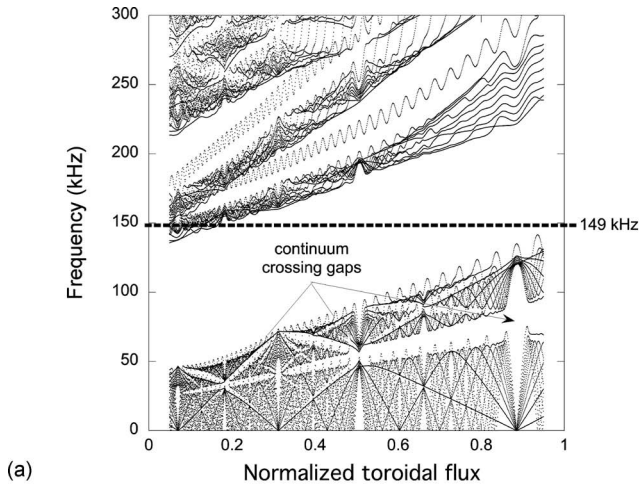
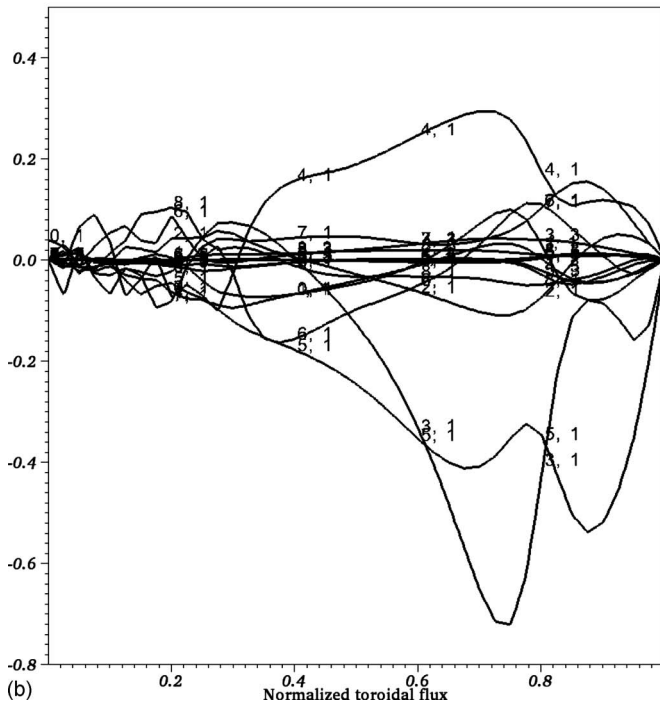


FIG. 15. (Color) Three-dimensional mode structure of QPS 149 kHz HAE mode.



(a)



(b)

FIG. 14. (a) Shear Alfvén continua for the $n=1$ mode family in QPS; (b) radial mode structure for a HAE mode at 149 kHz that exists in the large central open gap region.

$$\begin{aligned}
 & \left[\nabla \left(\frac{\mathbf{B} \cdot \nabla \tilde{\phi}}{B} \right) \right] \cdot \left[\nabla \left(\frac{\mathbf{B} \cdot \nabla \phi}{B} \right) \right] \\
 &= P \tilde{P} g^{\rho\rho} + Q \tilde{Q} g^{\theta\theta} + R \tilde{R} g^{\zeta\zeta} + (P \tilde{Q} + Q \tilde{P}) g^{\rho\theta} \\
 &+ (P \tilde{R} + R \tilde{P}) g^{\rho\zeta} + (Q \tilde{R} + R \tilde{Q}) g^{\zeta\theta}, \\
 & \left(\frac{\mathbf{B} \cdot \nabla \tilde{\phi}}{B} \right) \nabla \zeta \cdot \nabla \tilde{\phi} \times \nabla \left(\frac{J_{||0}}{B} \right) \\
 &= \frac{J^2 B^2}{\chi'} \left(\frac{\partial \phi}{\partial \zeta} + i \frac{\partial \phi}{\partial \theta} \right) \left[\frac{\partial \tilde{\phi}}{\partial \rho} \frac{\partial}{\partial \theta} \left(\frac{J_{||0}}{B} \right) - \frac{\partial \tilde{\phi}}{\partial \theta} \frac{\partial}{\partial \rho} \left(\frac{J_{||0}}{B} \right) \right],
 \end{aligned}$$

where

$$P = \frac{\partial J}{\partial \rho} \left(\frac{\partial \phi}{\partial \zeta} + i \frac{\partial \phi}{\partial \theta} \right) + J \frac{\partial^2 \phi}{\partial \rho \partial \zeta} + J i \frac{\partial^2 \phi}{\partial \rho \partial \theta} + J \frac{d}{d\rho} \frac{\partial \phi}{\partial \theta},$$

$$Q = \frac{\partial J}{\partial \theta} \left(\frac{\partial \phi}{\partial \zeta} + i \frac{\partial \phi}{\partial \theta} \right) + J \frac{\partial^2 \phi}{\partial \theta \partial \zeta} + J i \frac{\partial^2 \phi}{\partial \theta^2},$$

$$R = \frac{\partial J}{\partial \zeta} \left(\frac{\partial \phi}{\partial \zeta} + i \frac{\partial \phi}{\partial \theta} \right) + J \frac{\partial^2 \phi}{\partial \zeta^2} + J i \frac{\partial^2 \phi}{\partial \zeta \partial \theta},$$

$$J = \frac{\chi'}{B \sqrt{g}},$$

$$\frac{J_{||0}}{B} = \frac{J}{B \chi'} \left[I \left(\frac{\partial B_\rho}{\partial \zeta} - G' \right) - G \left(\frac{\partial B_\rho}{\partial \theta} - I' \right) \right],$$

$$B_\rho = -\frac{1}{g^{\rho\rho}} [g^{\rho\theta} B_\theta + g^{\rho\zeta} B_\zeta],$$

and \tilde{P} , \tilde{Q} , \tilde{R} are the same as above, but with ϕ replaced by $\tilde{\phi}$. The $g^{\rho\rho}$, $g^{\rho\theta}$, $g^{\rho\zeta}$, $g^{\theta\theta}$, etc. are the usual contravariant metric tensor elements for the coordinate system used here.

Using the Fourier/finite element representation given in Eq. (6), and separating out the ρ integrations over the rapidly varying finite element basis functions from the more slowly varying equilibrium coefficients, the inertia term matrix elements can be written as

$$\mathbf{G}_{ijpq} = \int \frac{d^3x}{v_A^2} \nabla \tilde{\phi} \cdot \nabla \phi$$

$$= A_{ijp} I_{pq}^{(1)} + B_{ijp} I_{pq}^{(2)} + C_{ijp} I_{pq}^{(3)} + D_{ijp} I_{pq}^{(4)},$$

where

$$A_{ijp} = \mu_0 n_{\text{ion}} \left\langle \cos_i \frac{g^{\rho\rho}}{B^2} \cos_j \right\rangle,$$

$$B_{ijp} = \mu_0 n_{\text{ion}} \left\langle \sin_i \frac{(n_i g^{\rho\zeta} - m_i g^{\rho\theta})}{B^2} \cos_j \right\rangle; \quad C_{ijp} = B_{jip},$$

$$D_{ijp} = \mu_0 n_{\text{ion}} \left\langle \sin_i \frac{[m_i m_j g^{\theta\theta} + n_i n_j g^{\zeta\zeta} - (n_i m_j + n_j m_i) g^{\theta\zeta}]}{B^2} \sin_j \right\rangle,$$

$$\cos_{i,j} \equiv \cos(m_{i,j}\theta - n_{i,j}\zeta); \quad \sin_{i,j} \equiv \sin(m_{i,j}\theta - n_{i,j}\zeta),$$

$$I_{pq}^{(1)} \equiv \int_0^1 d\rho f'_p f'_q; \quad I_{pq}^{(2)} \equiv \int_0^1 d\rho f_p f'_q;$$

$$I_{pq}^{(3)} \equiv \int_0^1 d\rho f'_p f_q; \quad I_{pq}^{(4)} \equiv \int_0^1 d\rho f_p f_q,$$

$$\langle a \rangle \equiv \int_0^{2\pi} d\zeta \int_0^{2\pi} d\theta \sqrt{g} a; \quad f' \equiv df/d\rho.$$

Using similar notation, the bending energy matrix is given as

$$\mathbf{F}_{ijpq} = \int \frac{d^3x}{v_A^2} \left[\nabla \left(\frac{\mathbf{B} \cdot \nabla \phi}{B} \right) \cdot \nabla \left(\frac{\mathbf{B} \cdot \nabla \tilde{\phi}}{B} \right) \right]$$

$$= E_{ijp} I_{pq}^{(1)} + F_{ijp} I_{pq}^{(2)} + G_{ijp} I_{pq}^{(3)} + H_{ijp} I_{pq}^{(4)}$$

$$+ K_{ijp} I_{pq}^{(2)} + L_{ijp} I_{pq}^{(4)},$$

where

$$k_{\parallel i} = n_i - im_i; \quad k_{\parallel j} = n_j - im_j,$$

$$E_{ijp} = \langle \sin_i g^{\rho\rho} J^2 k_{\parallel i} k_{\parallel j} \sin_j \rangle,$$

$$F_{ijp} = \left\langle \sin_i g^{\rho\rho} J k_{\parallel i} \frac{\partial}{\partial \rho} (J k_{\parallel j} \sin_j) \right\rangle$$

$$+ \left\langle \sin_i g^{\rho\theta} J k_{\parallel i} \frac{\partial}{\partial \theta} (J k_{\parallel j} \sin_j) \right\rangle$$

$$+ \left\langle \sin_i g^{\rho\zeta} J k_{\parallel i} \frac{\partial}{\partial \zeta} (J k_{\parallel j} \sin_j) \right\rangle,$$

$$G_{ijp} = F_{jip},$$

$$H_{ijp} = \left\langle g^{\rho\rho} \frac{\partial}{\partial \rho} (J k_{\parallel i} \sin_i) \frac{\partial}{\partial \rho} (J k_{\parallel j} \sin_j) \right.$$

$$+ \left. g^{\theta\theta} \frac{\partial}{\partial \theta} (J k_{\parallel i} \sin_i) \frac{\partial}{\partial \theta} (J k_{\parallel j} \sin_j) \right\rangle$$

$$+ \left\langle g^{\zeta\zeta} \frac{\partial}{\partial \zeta} (J k_{\parallel i} \sin_i) \frac{\partial}{\partial \zeta} (J k_{\parallel j} \sin_j) \right\rangle + H_{ijp}^{(1)} + H_{jip}^{(1)},$$

$$H_{ijp}^{(1)} = \left\langle g^{\rho\theta} \frac{\partial}{\partial \rho} (J k_{\parallel i} \sin_i) \frac{\partial}{\partial \theta} (J k_{\parallel j} \sin_j) \right.$$

$$+ \left. g^{\rho\zeta} \frac{\partial}{\partial \rho} (J k_{\parallel i} \sin_i) \frac{\partial}{\partial \zeta} (J k_{\parallel j} \sin_j) \right\rangle$$

$$+ \left\langle g^{\zeta\theta} \frac{\partial}{\partial \theta} (J k_{\parallel i} \sin_i) \frac{\partial}{\partial \zeta} (J k_{\parallel j} \sin_j) \right\rangle,$$

$$K_{ijp} = \left\langle \frac{J^2 B^2}{\chi'} k_{\parallel i} \frac{\partial}{\partial \theta} \left(\frac{J_{\parallel 0}}{B} \right) \sin_i \cos_j \right\rangle;$$

$$L_{ijp} = \left\langle \frac{J^2 B^2}{\chi'} k_{\parallel i} m_j \frac{\partial}{\partial \rho} \left(\frac{J_{\parallel 0}}{B} \right) \sin_i \sin_j \right\rangle.$$

The evaluation of the above matrix elements is then completed using Fourier expansions for the contravariant metric tensor elements. These metric elements are formed in the usual way by first calculating the covariant metric elements and then inverting their matrix. The covariant elements are obtained from

$$g_{ij} = \vec{e}_i \cdot \vec{e}_j \quad \text{with} \quad \vec{e}_i = \frac{\partial \vec{r}}{\partial \alpha_i}; \quad \vec{r} = (R, \phi, z); \quad \text{and}$$

$$\alpha = (\rho, \theta, \zeta).$$

R , ϕ , and z are represented as

$$R = \sum R_{mn}(\rho) \cos(m\theta - n\zeta);$$

$$z = \sum z_{mn}(\rho) \sin(m\theta - n\zeta),$$

$$\phi = \zeta + \sum \phi_{mn}(\rho) \sin(m\theta - n\zeta).$$

Using Fourier expansions for the contravariant metric elements obtained from the above expressions, the surface integrals in the matrix elements can be evaluated using the techniques of transforming to real space, taking products of periodic coefficients, then transforming back to Fourier space and doing the final integrations (involving products of three Fourier terms) analytically, as has been described previously in Ref. 11.

¹A. Weller, D. A. Spong, R. Jaenicke, A. Lazaros, F. P. Penningsfeld, S. Sattler, W7-AS Team, and NBI Group, *Phys. Rev. Lett.* **72**, 1220 (1994).

²M. Isobe, K. Toi, H. Matsushita, M. Isobe, K. Toi, H. Matsushita, K. Goto, C. Suzuki, K. Nagaoka, N. Nakajima, S. Yamamoto, S. Murakami, A. Shimizu, Y. Yoshimura, T. Akiyama, T. Minami, M. Nishiura, S. Nishimura, D. S. Darrow, D. A. Spong, K. Shinohara, M. Sasao, K. Matsuoka, S. Okamura, and the CHS team, *Nucl. Fusion* **46**, S918 (2006).

³K. Toi, S. Yamamoto, N. Nakajima, S. Ohdachi, S. Sakakibara, M. Osakabe, S. Murakami, K. Y. Watanabe, M. Goto, K. Kawahata, Y. I.

- Kolesnichenko, S. Masuzaki, S. Morita, K. Narihara, Y. Narushima, Y. Takeiri, K. Tanaka, T. Tokuzawa, H. Yamada, I. Yamada, K. Yamazaki, and LHD Experimental Group, *Plasma Phys. Controlled Fusion* **46**, S1 (2004).
- ⁴R. Jimenez-gomez, E. Ascasibar, T. Estrada, I. García-Cortés, B. Van Milligen, A. López-Fraguas, I. Pastor, and D. López-Bruna, *Fusion Sci. Technol.* **51**, 20 (2007).
- ⁵S. Yamamoto, K. Nagasaki, Y. Suzuki, T. Mizuuchi, H. Okada, S. Kobayashi, B. Blackwell, K. Kondo, G. Motojima, N. Nakajima, Y. Nakamura, C. Nührenberg, Y. Torii, S. Watanabe, and F. Sano, *Fusion Sci. Technol.* **51**, 92 (2007).
- ⁶C. Deng, D. L. Brower, B. N. Breizman, D. A. Spong, A. F. Almagri, D. T. Anderson, F. S. B. Anderson, W. X. Ding, W. Guttenfelder, K. M. Likin, and J. N. Talmadge, *Phys. Rev. Lett.* **103**, 025003 (2009).
- ⁷W. W. Heidbrink, *Phys. Plasmas* **9**, 2113 (2002).
- ⁸C. Z. Cheng and M. S. Chance, *J. Comput. Phys.* **71**, 124 (1987).
- ⁹A. Könies, *Phys. Plasmas* **7**, 1139 (2000).
- ¹⁰M. Nool and A. van der Ploeg, *SIAM J. Sci. Comput. (USA)* **22**, 95 (2000).
- ¹¹D. A. Spong, R. Sanchez, and A. Weller, *Phys. Plasmas* **10**, 3217 (2003).
- ¹²C. Nührenberg, *Phys. Plasmas* **6**, 137 (1999).
- ¹³S. E. Kruger, C. C. Hegna, and J. D. Callen, *Phys. Plasmas* **5**, 4169 (1998).
- ¹⁴A. H. Boozer, *Phys. Fluids* **24**, 1999 (1981).
- ¹⁵D. A. Spong, B. A. Carreras, and C. L. Hedrick, *Phys. Fluids B* **4**, 3316 (1992).
- ¹⁶E. Anderson, Z. Bai, C. Bischof *et al.*, *LAPACK User's Guide*, 3rd ed. (Society for Industrial and Applied Mathematics, Philadelphia, PA, 1999).
- ¹⁷G. L. G. Sleijpen and H. A. Van der Vorst, *SIAM Rev.* **42**, 267 (2000). Code for this algorithm is available at M. E. Hochstenbach. Jacobi-Davidson Gateway: <http://www.win.tue.nl/casa/research/topics/jd/index.html>.
- ¹⁸*Templates for the Solution of Algebraic Eigenvalue Problems: A Practical Guide*, edited by Z. Bai, J. Demmel, J. Dongarra, A. Ruhe, and H. van der Vorst (SIAM, Philadelphia, PA, 2000).
- ¹⁹C. B. Moler and G. W. Stewart, *SIAM (Soc. Ind. Appl. Math.) J. Numer. Anal.* **10**, 241 (1973).
- ²⁰M. Osakabe, S. Yamamoto, K. Toi, Y. Takeiri, S. Sakakibara, K. Nagaoka, K. Tanaka, K. Narihara, and the LHD Experimental Group, *Nucl. Fusion* **46**, S911 (2006).
- ²¹Y. Todo, N. Nakajima, M. Osakabe, S. Yamamoto, and D. A. Spong, *Proceedings of the 22nd IAEA Fusion Energy Conference*, Geneva, Switzerland, 2008, edited by G. Mank (International Atomic Energy Agency, Vienna, Austria, 2008).
- ²²W. A. Cooper, G. Y. Fu, S. Gruber, S. Merazzi, U. Schwenn, and D. V. Anderson, *Theory of Fusion Plasmas, Proceedings of the Joint Varenna-Lausanne International Workshop*, Varenna, Italy, 1990 (Editrice Compositori, Bologna, Italy, 1990), p. 655.
- ²³K. Toi, F. Watanabe, T. Tokuzawa, K. Ida, S. Morita, T. Ido, A. Shimizu, M. Isobe, K. Ogawa, D. Spong, Y. Todo, T. Watari, S. Ohdachi, S. Sakakibara, S. Yamamoto, S. Inagaki, K. Narihara, M. Osakabe, K. Nagaoka, Y. Narushima, K. W. Watanabe, H. Funaba, M. Goto, K. Ikeda, T. Ito, O. Kaneko, S. Kubo, T. Minami, J. Miyazawa, Y. Nagayama, M. Nishiura, Y. Oka, R. Sakamoto, T. Shimoza, Y. Takeiri, K. Tanaka, K. Tsumori, I. Yamada, M. Yoshinuma, K. Kawahata, A. Komori, and LHD Experimental Group, *Proceedings of the 22nd IAEA Fusion Energy Conference*, Geneva, Switzerland, 2008, edited by G. Mank (International Atomic Energy Agency, Vienna, Austria, 2008).
- ²⁴S. Yamamoto, K. Toi, N. Nakajima, S. Ohdachi, S. Sakakibara, K. Y. Watanabe, M. Goto, K. Ikeda, O. Kaneko, K. Kawahata, S. Masuzaki, T. Morisaki, S. Morita, S. Murakami, K. Narihara, Y. Oka, M. Osakabe, Y. Takeiri, K. Tanaka, T. Tokuzawa, K. Tsumori, H. Yamada, I. Yamada, K. Yamazaki, and LHD Experimental Group, *Phys. Rev. Lett.* **91**, 245001 (2003).
- ²⁵Y. V. Yakovenko, A. Weller, A. Werner, S. Zegenhagen, O. P. Fesenyuk, and Y. I. Kolesnichenko, *Plasma Phys. Controlled Fusion* **49**, 535 (2007).